RSC Advances

PAPER

View Article Online
View Journal | View Issue

Cite this: *RSC Adv.*, 2026, **16**, 27069

Synthesis of magnetic adsorbents from bamboo fiber functionalized with ferrite–SiO_2-PEI for efficient dye removal in wastewater treatment

Ratchaneekorn Kampangta,[a] Chomsri Siriwong,[a] Narubeth Lorwanishpaisarn,[b] Kingkaew Chayakul Chanapattharapol [a] and Poonsuk Poosimma *[a]

Consistent with the growing concern over dye pollution, this study reports the successful synthesis of $CuFe_2O_4$ and $NiFe_2O_4$ *via* the sol–gel method, followed by silica coating and surface modification with polyethyleneimine (PEI). Magnetic bamboo fiber composites (MBF) were created by effectively depositing $CuFe_2O_4$–SiO_2-PEI and $NiFe_2O_4$–SiO_2-PEI on bamboo fibers. The resulting MBF-Cu and MBF-Ni demonstrated improved surface functionality, strong thermal stability, and soft magnetic properties, making them suitable for use as filters for removing dye pollutants from industrial wastewater. The MBF-Ni composite was applied as a fixed-bed column for dye removal, demonstrating excellent performance in eliminating Congo Red (CR) compared with Methylene Blue (MB) and Methyl Orange (MO). The MBF-Ni filter effectively removed CR at a concentration of 10 mg L^{-1} with removal efficiency and adsorption capacity reaching 90.90% and 2.56 mg g^{-1}, respectively. In addition, MBF-Ni has shown adsorption follows pseudo-second-order kinetics with k_2 = 0.0297 (min) and q_e at 5.83 (mg g^{-1}). Overall, MBF-Ni presents a promising, eco-friendly material for the efficient removal of dye pollutants from industrial wastewater, offering potential for broad-scale filtration and environmental applications.

Received 26th December 2025
Accepted 8th May 2026

DOI: 10.1039/d5ra10014c

rsc.li/rsc-advances

1 Introduction

The rapid expansion of industrial activities, particularly in textile and printing sectors, has led to the widespread discharge of synthetic dyes into aquatic environments.[1] Many synthetic dyes are chemically stable, non-biodegradable, and potentially toxic.[2]

Congo red (CR) and methylene blue (MB) are frequently detected in industrial wastewater due to their extensive commercial use. CR belongs to the azo dye family, containing the characteristic –N=N– functional group, whereas MB is a cationic dye with a heterocyclic aromatic structure.[3] This variation enables systematic investigation of adsorption selectivity and underlying mechanisms, particularly electrostatic interactions between the adsorbent surface and dye molecules.[4] In addition, the molecular structures and sizes of these dyes differ significantly, with CR having a relatively large and complex structure while MB possesses a medium-sized aromatic framework.

Ferrite nanoparticles are a class of magnetic nanomaterials composed of iron oxide combined with divalent metal ions, typically represented by the general formula MFe_2O_4 (where M = Co, Ni, Zn, Mn, *etc.*). Owing to their nanoscale size, they exhibit unique properties such as ferromagnetism, high surface area, and good chemical stability. These characteristics make ferrite nanoparticles highly attractive for a wide range of applications, including biomedical fields, environmental remediation, catalysis, pollutant adsorption and magnetic separation.[5,6] Silica (SiO_2) coating ferrite particles also keeps them magnetically sensitive and lowers the chance of agglomeration, both of which are critical for separation and recycling procedures.[7] In addition to improving colloidal stability and providing a wealth of hydroxyl groups for further surface functionalization, the SiO_2 shell serves as a protective barrier.[8] M. Gharagozlou *et al.* (2023)[9] studied magnetic ferrite@SiO_2 systems in dye removal from aqueous solution due to their magnetic separability, high stability, and enhanced adsorption capacity. The ferrite core enables easy recovery, while the SiO_2 shell improves dispersibility and provides active sites for pollutant removal.

Polyethyleneimine (PEI), was coated onto SiO_2 to introduce abundant amine functional groups, enhance electrostatic interactions with anionic pollutants, and improve dispersion and adsorption performance while retaining magnetic separability.[10] Kapilov Buchman *et al.* (2013)[11] synthesis the PEI coated onto SiO_2 nanoparticles, possess high positive charge density due to the presence of ammonium (NH_4^+) ions. For separation applications, improves electrostatic interaction with dyes.[12]

[a]*Materials Chemistry Research Center, Department of Chemistry and Center of Excellence for Innovation in Chemistry, Faculty of Science, Khon Kaen University, Khon Kaen 40002, Thailand. E-mail: ppoons@kku.ac.th*

[b]*Department of Biotechnology, Faculty of Technology, Khon Kaen University, Khon Kaen 40002, Thailand*

Bamboo is a fast-growing, renewable plant belonging to the Poaceae family, widely distributed in tropical and subtropical regions.[13] It has attracted considerable attention as a sustainable material due to its low cost, environmental friendliness, and abundant availability. Bamboo fibers possess a porous architecture and high surface area, making them highly suitable for adsorption applications. However, a lot of solid waste is produced during the processing of bamboo, including dust, shavings, fiber scraps, and other unusable byproducts. On the other hand, the fact that bamboo given high cellulose content, biodegradability, low cost, and structural versatility,[14] which offers a promising alternative raw material for the development of eco-friendly composites, adsorbents, and catalysts.[15] To enhance the performance and surface activity of bamboo fibers, surface modification and hybridization with functional nanomaterials have been widely explored. Y. Miyah *et al.* (2020)[16] use naturel materials (Corn cob and Walnut shells) and ferrite nanoparticle to eliminated methylene blue (MB) from wastewater through developing high-performance filters. This strategy not only improves water quality but also provides a practical and sustainable solution for minimizing environmental pollution before releasing treated water into natural ecosystems.

This work aims to synthesis copper ($CuFe_2O_4$) and nickel ($NiFe_2O_4$) ferrite nanoparticles, coating in a SiO_2 shell, and then modifying with PEI. The products $CuFe_2O_4$–SiO_2-PEI and $NiFe_2O_4$–SiO_2-PEI were used to create a multifunctional hybrid material modified bamboo fibers (MBF) by functionalizing on bamboo fibers. MBF-Cu and MBF-Ni have superior surface functionality, due magnetic characteristics, and potential for environmental uses. However, with its efficiency and chemical stability of MBF-Ni, we applied the MBF-Ni to use as filter for dyes removal in wastewater treatment applications (Scheme 1). In addition, it is also considered to demonstrates the innovative conversion of natural waste into useful materials with special qualities that have enormous promise for future development and use in a variety of industries.

1.1 Introducing sample names

ABF: alkali treated bamboo fibers.

MBF: multifunctional hybrid material modified bamboo fibers.

MBF-Cu: multifunctional hybrid material modified bamboo fibers by $CuFe_2O_4$–SiO_2-PEI.

MBF-Ni: multifunctional hybrid material modified bamboo fibers by $NiFe_2O_4$–SiO_2-PEI.

2 Experimental

2.1 Materials

Copper(II) acetate monohydrate ($Cu(C_2H_3O_2)_2 \cdot H_2O$) and tetraethyl orthosilicate (TEOS) 98% were purchased from SIGMA-ALDRICH. Nickel nitrate hexahydrate ($Ni(NO_3)_2 \cdot 6H_2O$). Iron nitrate hydrate ($Fe(NO_3)_3 \cdot 9H_2O$) and Ethylene glycol were purchased from QReC^R. Citric acid monohydrate ($C_6H_8O_7 \cdot H_2O$) was purchased from TPC. Ammonia solution (NH_4OH) was purchased from ANaPURER. Hydrogen peroxide (H_2O_2) and absolute ethanol (98%) were purchased from RCI Labscan. Polyethylenimine (PEI) branched 99% with a mass average molecular weight of 10 000 was purchased from ACROS ORGANICS. Methyl Orange Indicator ($C_{14}H_{14}N_3NaO_3S$) was purchased from RCI Labscan. Congo Red Indicator ($C_{32}H_{22}N_6Na_2O_6S_2$) was purchased from LOBA Chemie. Methylene Blue Indicator ($C_{16}H_{18}ClN_3S$) was purchased from Riedel-de Haën. All aqueous solutions were prepared using deionized water and other reagents were used in analytical grade.

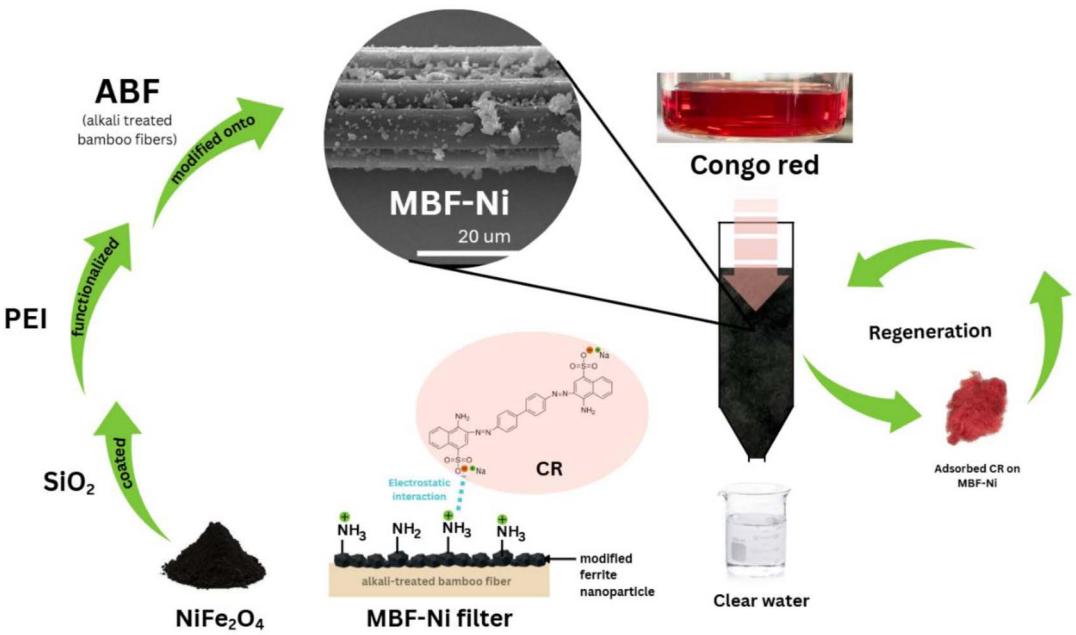

Scheme 1 Application of MBF-Ni using as column filter for Congo Red (CR) filtration.

2.2 Characterization

The surface morphology of ferrite nanoparticles and modified bamboo fibers was observed using desktop scanning electron microscopes (MiniSEM), model SEC-SNE 4500M. The crystalline structure was determined using X-ray diffractometer (XRD), model PANalytical-EMPYREAN. Thermogravimetric (TGA) and differential thermal analysis (DTG) of samples was investigated using STA-449 F5 Jupiter. The surface chemical composition was investigated using X-ray Photoelectron Spectroscopy (XPS). The functional groups were determined using Fourier transform infrared spectroscopy (FT-IR), model Bruker-TENSOR27. The magnetic behavior of the composite was investigated using a Vibrating Sample Magnetometer (VSM). The absorbance of dyes was investigated using UV-VIS Spectrophotometer, model SP-UV300.

2.3 Synthesis of copper ferrite nanoparticles ($CuFe_2O_4$) and nickel ferrite nanoparticles ($NiFe_2O_4$)

Copper ferrite nanoparticles and Nickel ferrite nanoparticles were synthesized though sol–gel method by following the work of Verma *et al.* (2024).[17] In a typical synthesis, 80.8 g of $Fe(NO_3)_3\cdot 9H_2O$ and 24.16 g of $Cu(C_2H_3O_2)_2\cdot H_2O$ were dissolved into deionized water one by one. Then, $Fe(NO_3)_3\cdot 9H_2O$ solution was mixed with $Cu(C_2H_3O_2)_2\cdot H_2O$ solution under magnetic stirring for 1 h. Citric acid monohydrate solution (57.7 g) was added and continuous stirring for 30 min. For synthesis of nickel ferrite nanoparticles, the solution of $Fe(NO_3)_3\cdot 9H_2O$ (80.8 g) and $Ni(NO_3)_2\cdot 6H_2O$ (29.0 g) were prepared. Then, $Fe(NO_3)_3\cdot 9H_2O$ was mixed with $Ni(NO_3)_2\cdot 6H_2O$ under magnetic stirring for 1 h. Citric acid monohydrate solution (63.0 g) was added to the mixed solution and continuous stirring for 30 min. After preparing both of two substances, 10 mL of ethylene glycol and 5 mL of H_2O_2 was slowly added followed by order. Stir the two evenly mixed solutions at 250 °C for 1 h. Then, refluxed for 2 h. After that, the mixed solutions were filled on a Buchner funnel and washed with deionized water until the pH reached about 7. Then, dried at 60 °C in an air-drying oven for 24 h. Finally, copper ferrite particles and nickel ferrite particles were obtained after sintering at 1000 °C for 4 h.

2.4 Synthesis of silica core–shell copper ferrite nanoparticles ($CuFe_2O_4$–SiO_2) and silica core–shell nickel ferrite nanoparticles ($NiFe_2O_4$–SiO_2)

Ferrite nanoparticles were coated with silica (SiO_2). 1 g of calcined $CuFe_2O_4$ and $NiFe_2O_4$ were dispersed in 50 mL of 95% ethanol and ultrasonically distributed for 30 min. Then, 9 mL of NH_4OH and 2.5 mL of TEOS solution were added consecutively to the above suspensions. Stir the mixtures at room temperature for 10 h. The mixed solutions were then placed on a Buchner funnel and washed with deionized water until the pH reached about 7. Finally, dried at 60 °C in an air-drying oven for 24 h.

2.5 Synthesis of coated copper ferrite nanoparticles ($CuFe_2O_4$–SiO_2-PEI) and coated nickel ferrite nanoparticles ($NiFe_2O_4$–SiO_2-PEI)

0.016 g of polyethylenimine (PEI) was dissolved in 1.5 mL of deionized water (prepare 2 sets). Then, 0.75 g of $CuFe_2O_4$–SiO_2 and $NiFe_2O_4$–SiO_2 were dissolved into 35 mL of deionized water one by one. After that, PEI solution was mixed with $CuFe_2O_4$–SiO_2 and $NiFe_2O_4$–SiO_2, the mixtures were stirred at room temperature for 12 h.

2.6 Synthesis of magnetic composite (MBF-Cu and MBF-Ni)

0.4 g of ABF (with length 0.5–1 cm, diameter 12.24–17.32 μm)[18] was dissolved in 200 mL of deionized water (prepare 2 sets). Then, $CuFe_2O_4$–SiO_2-PEI and $NiFe_2O_4$–SiO_2-PEI solution from above procedure were added to ABF suspension one by one. NH_4OH was added dropwise into mixtures until the pH ~9 and stirred under ambient temperature for 4 h. After that, mixed solutions were filled on a Buchner funnel. Finally, kept the modified bamboo fibers (MBF-Cu and MBF-Ni) at 60 °C in an air-drying oven for 24 h.

2.7 Chemical stability test

MBF-Cu and MBF-Ni were immersed in various solvents including, ethyl acetate, hexane, diethyl ether, toluene, dichloromethane (DCM), acetonitrile (ACN), DI water, ethanol, methanol, *N*,*N*-dimethylformamide (DMF) and hydrochloric acid (HCl) for 24 h. Then using XRD to confirm chemical stability of the samples.

2.8 Optimization condition of prepared-column for dyes filtration

For applications in dye filtration, ABF and MBF-Ni were used as filter in column. A standard stock solution 500 mg per L CR, MO and MB were used to make 20 mg per L CR, MO and MB solution. Then each dye was passed through the columns (diameter of 0.5 cm, height of filter bed fixed at 4 cm) under batch system by volume of 20 mL. Finally, detect absorbances using UV-vis spectroscopy (photometric mode) and set the maximum wavelengths (λ_{max}) for MB, MO and CR at 662, 464, and 498 nm, respectively.

2.9 Effect of solution volume and concentration of CR for filtration efficiency

The columns (with diameter 0.5 cm) were varying height of each filter with 1, 2, 4 and 6 cm (weight 0.040, 0.075, 0.15 and 0.35 g), respectively. The selectivity of filters for remove MB, MO and CR, 20 mL of dyes solutions (20 mg L^{-1} dyes) was passing through a filter in column under batch system. Effect of solution volume and concentration of CR for filtration efficiency, using 10, 20, 50, and 100 mg L^{-1}. Then each concentration was passed through the column of MBF-Ni filter (diameter of 0.5 cm, height of filter bed fixed at 4 cm) by volume of 10, 20, 30, and 50 mL, respectively. Lastly, the absorbance of dyes was detected by UV-vis spectroscopy (scan mode).

2.10 Removal efficiency and adsorption capacity of MBF-Ni filter

CR solutions were varying concentrations with 10, 20, 50, and 100 mg L^{-1}, 50 mL of these were passed through column fixed height 4 cm of MBF-Ni filter under batch system. Then, the

absorbance of dyes was detected by UV-vis spectroscopy (scan mode) using the maximum wavelengths (λ_{max}) for CR at 498 nm.

2.11 Regeneration of ABF and MBF-Ni filter

ABF filter after use was regeneration by immersed in 0.1 M HCl solution, and MBF-Ni was immersed in 0.1 M NaCl solution, respectively. Soaking for 60 min then wash each filter with 50% v/v ethanol, follow sonicate for 15 min. After that wash with DI water until pH ~7. Finally, dried at 60 °C in oven for 24 h.

2.12 Adsorption kinetics and isotherm

The adsorption experiments were carried out using Congo Red (CR) and Methylene Blue (MB) as model dye pollutants.[19] Stock solutions of both dyes were first prepared and subsequently diluted to obtain a series of dyes solutions (25 mL) with different initial concentrations of 10, 20, 50, and 100 mg L^{-1}. For each experiment, 0.05 g of adsorbent, namely ABF and MBF-Ni, was accurately weighed and added into separate flasks containing the prepared dye solutions. Then, stir at constant temperature and take samples at different times (at 10, 20, 30, 40, 50, 60 min). Finally, absorbances were determined using UV-vis spectroscopy (photometric mode) and set the maximum wavelengths (λ_{max}) for MB and CR set at 662 and 498, respectively.

3 Results and discussion

3.1 Morphological and structural characteristics

Desktop scanning electron microscopes was used for determining morphology and structure of ferrite nanoparticle and modified bamboo fibers. In Fig. 1a, the calcined Cu Fe_2O_4 particles exhibit an aggregated and irregular morphology with relatively large, rough-surfaced particles.[20] This morphology is typical for spinel ferrites synthesized *via* co-precipitation or sol–gel methods. After coating by SiO_2 as show in Fig. 1b, the surface of particles appears significantly rougher, which indicating successful deposition of the silica layer.[21] The creation of polymeric networks from the PEI coating may be the cause of the slightly more aggregated particles and more irregular surface features seen in Fig. 1c after PEI treatment. Finally, the MBF-Cu sample (Fig. 1d) shows fibrous structures with a smooth backbone and visible deposition of Cu-containing particles along the fibers surface. This structure is indicative of fibrous framework for $CuFe_2O_4$ deposition.[22] In Fig. 2a, $NiFe_2O_4$ exhibits relatively well-faceted large grains. The observed porosity is primarily attributed to the evaporation of gases released during the synthesis process.[23] $NiFe_2O_4$–SiO_2 in Fig. 2b exhibits a more compact surface because of silica. The rougher and more porous shape of $NiFe_2O_4$–SiO_2-PEI as show in Fig. 2c is advantageous for improving surface reactivity.[24] In Fig. 2d can confirms the adherence of nickel ferrite particles on the bamboo fibers. These morphological transformations confirm the sequential functionalization and support integration process. This morphology offers increased surface area and porosity, which are beneficial for applications such as catalysis or adsorption.[25]

3.2 Thermal properties

The thermogravimetric analysis (TGA) was used for determining thermal stability, composition and decomposition behavior of

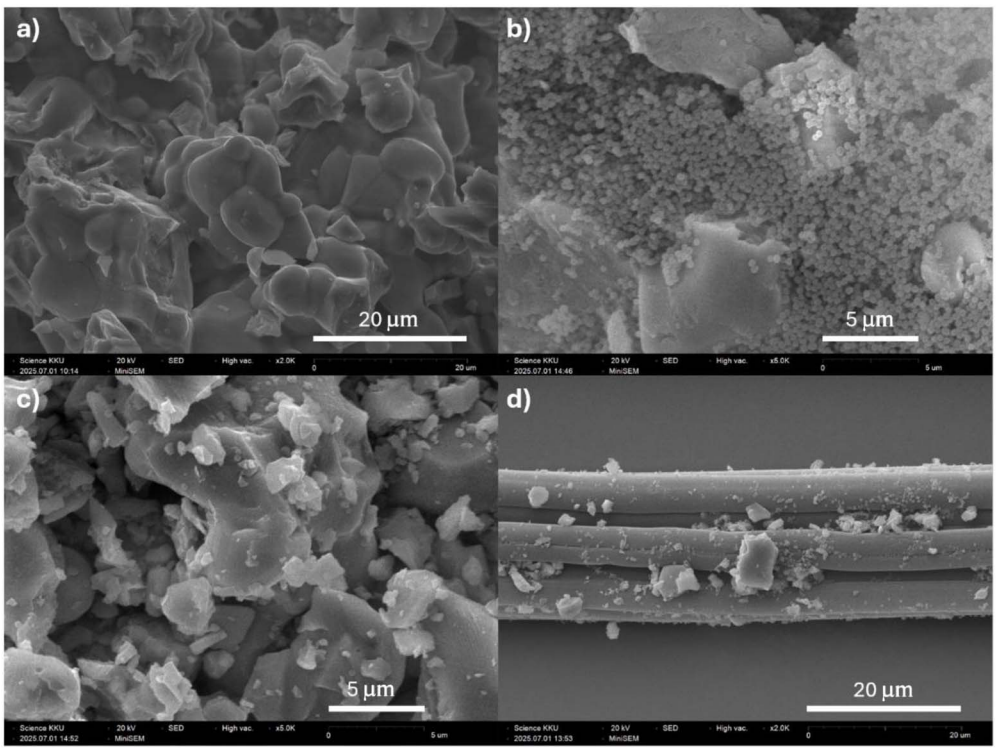

Fig. 1 SEM images of (a) $CuFe_2O_4$, (b) $CuFe_2O_4$–SiO_2, (c) $CuFe_2O_4$–SiO_2-PEI, and (d) MBF-Cu.

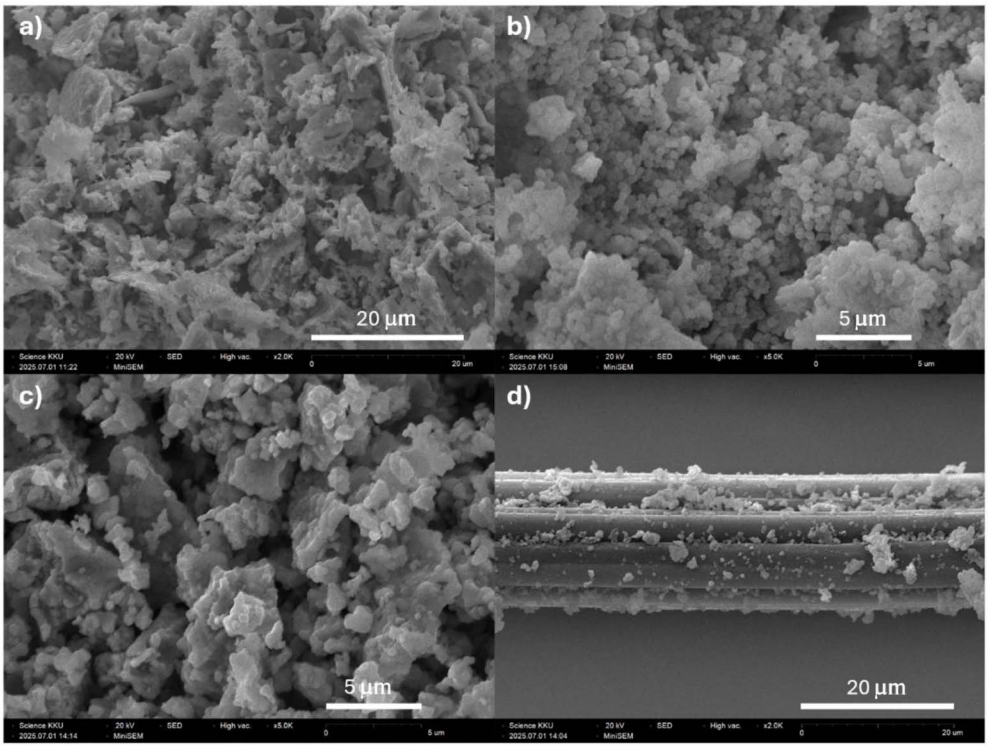

Fig. 2 SEM images of (a) $NiFe_2O_4$, (b) $NiFe_2O_4$–SiO_2, (c) $NiFe_2O_4$–SiO_2-PEI, and (d) MBF-Ni.

materials. Fig. 3a, MBF-Cu, MBF- Ni and ABF exhibit a multistep weight loss pattern upon heating from 30 to 600 °C, which corresponds to the decomposition and removal of organic components and other volatile substances. In the TGA curves (Fig. 3a), the MBF-Cu and MBF-Ni samples show relatively similar thermal behavior. The initial slight weight decreases from 30 to 100 °C can be attributed to the evaporation of absorbed water on fibers.[26] The major weight loss of the MBF-Cu and MBF-Ni occurs between 250-350 °C, indicating the decomposition of polysaccharide derived from the bamboo fibers.[27] The loading degree of ferrite nanoparticles on bamboo fibers was calculated using the following eqn (1),[28]

$$\text{Loading degree (\%)} = ((\text{MF} - \text{UMF})/\text{MF}) \times 100 \quad (1)$$

where MF and UMF is the content of modified bamboo fibers and an unmodified bamboo fiber, respectively.

In Table 1 shows the final weight, loading degree and degradation temperature of MBF-Cu, MBF-Ni, and ABF. At 600 °C, the residual mass of MBF-Cu and MBF-Ni increased from 14.72% to 58.36% and 58.87%, respectively. This result suggesting successful incorporation of metal species onto the bamboo fibers with moderate thermal stability.[19] The ABF sample show a significantly higher weight loss than MBF samples, indicating a much larger content of organic matter, and the absence of metal ions.

The DTG curves in Fig. 3b show three endothermic peaks, which corresponding to the maximum decomposition rate. The peak of MBF-Cu, MBF-Ni and ABF shows temperature 321.34 °C, 337.34 °C and 331.33 °C, respectively. The decomposition temperatures of the samples don't have any effect on the thermal stability of the bamboo fibers because of metal ions.[20,21] From the result, the MBF-Ni exhibits the highest decomposition temperature, indicating that Ni species and bamboo fibers interact more effectively.

3.3 Crystalline structure

The XRD patterns confirm the successful synthesis and preservation of ferrite nanoparticles. The diffraction peaks of $CuFe_2O_4$ pattern, correspond the phase of copper ferrite (JCPDS No. 34-0425).[29] As show in Fig. 4a, characteristic reflections of as-prepared $CuFe_2O_4$ (black curve) appear at $2\theta = 30.2°$, 34.8°, 35.6°, 36.7°, 43.3°, 53.6°, 57.2°, and 62.9°, which are indexed to the (220), (310), (311), (222), (400), (422), (511), and (440) planes, respectively. For as-prepared $NiFe_2O_4$ (Fig. 4b), the XRD pattern displays sharp and well-defined peaks at $2\theta = 30.3°$, 35.7°, 36.9°, 43.4°, 53.8°, 57.3°, and 63.0°, which are indexed to the (220), (311), (222), (400), (422), (511), and (440) planes of the spinel-type $NiFe_2O_4$ structure (JCPDS No. 10-0325).[30] After calcination of $CuFe_2O_4$ and $NiFe_2O_4$ (red curves), the crystallinity of $CuFe_2O_4$ and $NiFe_2O_4$ increases, as evidenced by the sharper and more intense peaks, which indicates enhanced crystallite growth and structural ordering upon heat treatment.[31] In the $CuFe_2O_4$–SiO_2 and $NiFe_2O_4$–SiO_2 (pink curves), $CuFe_2O_4$–SiO_2-PEI and $NiFe_2O_4$–SiO_2-PEI (blue curves) sample, the presence of silica and PEI does not introduce new crystalline phases, indicating that the functionalization is mainly on the surface without affecting the bulk structure. The XRD patterns of MBF-Cu and MBF-Ni (green curves) show the main peaks as mentioned earlier. In addition, a single broad peak around 22.1° 2θ was suggested to the amorphized cellulose of fibers.[32]

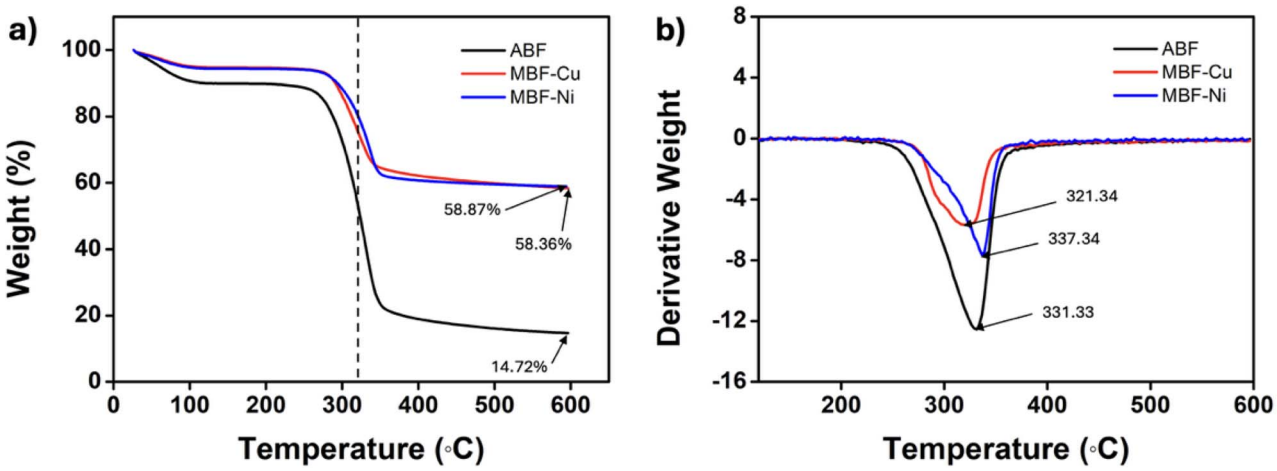

Fig. 3 (a) TGA and (b) DTG curves of MBF-Cu, MBF-Ni, and ABF.

Table 1 Final weight, loading degree and degradation temperature of MBF-Cu, MBF-Ni, and ABF

Sample	Final weight (%)	Loading degree (%)	Degradation temperature (°C)
MBF-Cu	58.36	43.64	321.34
MBF-Ni	58.87	44.15	337.34
ABF	14.72	—	331.33

3.4 Functional group analysis

The FT-IR spectra of the functionalized magnetic bamboo fibers (MBF) and their respective components are shown in Fig. 5a and b, all samples display a broad absorption band in the range of 3200–3500 cm^{-1}, which is attributed to overlapping O–H and N–H stretching vibrations, indicating the presence of hydroxyl groups and amines from both the natural biofibers and PEI.[33] The bands near 2920 cm^{-1} and 2850 cm^{-1} correspond to asymmetric and symmetric C–H stretching vibrations, respectively. In the spectra of the MBF-Cu and MBF-Ni (red curves) and ABF (blue curves). A peak observed near 1650 cm^{-1} can be assigned to the C=O stretching (amide I) or C=C stretching,[34] suggest the presence of proteinaceous material or unsaturated bonds in the biomass matrix. Additional bands around 1100 cm^{-1} are attributed to Si–O–Si stretching vibrations,[35,36] confirming the successful coating of the ferrite nanoparticles with a silica shell. Crucially, the spectra of the $CuFe_2O_4$–SiO_2-PEI and $NiFe_2O_4$–SiO_2-PEI (black curves) show strong absorption bands below 600 cm^{-1}, which are assigned to metal–oxygen (M-O) stretching vibrations in the ferrite lattice,[29,37] such as Fe–O, Cu–O, and Ni–O. These bands confirm the presence of the spinel ferrite phase in the final composites.

3.5 Elemental composition analysis

The elemental composition and oxidation states of the synthesized materials were examined using X-ray photoelectron spectroscopy (XPS). In Fig. 6a displays the wide-scan XPS

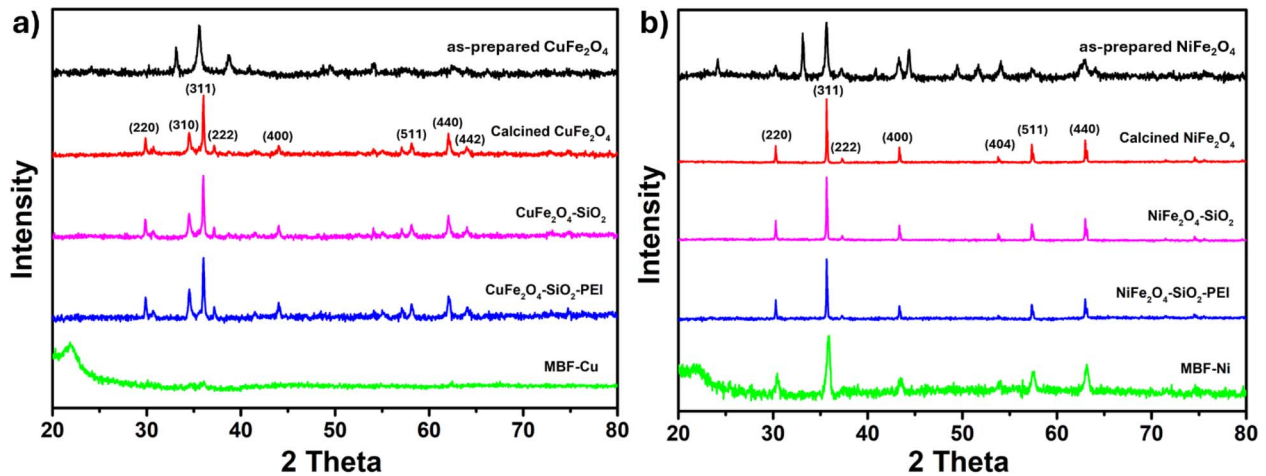

Fig. 4 XPS spectra of (a) as-prepared $CuFe_2O_4$, calcined $CuFe_2O_4$, $CuFe_2O_4$–SiO_2, $CuFe_2O_4$–SiO_2-PEI, and MBF-Cu, (b) as-prepared $NiFe_2O_4$, calcined $NiFe_2O_4$, $NiFe_2O_4$–SiO_2, $NiFe_2O_4$–SiO_2-PEI, and MBF-Ni.

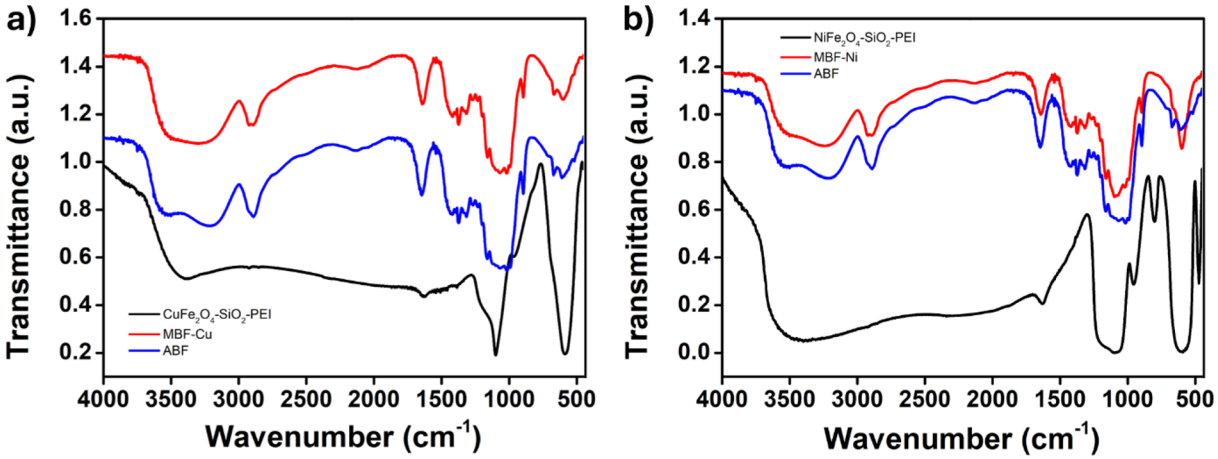

Fig. 5 FT-IR spectra of (a) $CuFe_2O_4$–SiO_2-PEI, MBF-Cu, and ABF, (b) $NiFe_2O_4$–SiO_2-PEI, MBF-Ni, and ABF.

spectra of $CuFe_2O_4$ and MBF-Cu, revealing the presence of Cu, Fe, O, and C in both samples. Similarly, Fig. 6b confirms the presence of Ni, Fe, O, and C in $NiFe_2O_4$ and MBF-Ni. The decrease in signal intensity and minor peak shifts observed in the MBF-Cu and MBF-Ni suggest surface modification or interaction between the modified ferrite nanoparticles and the bamboo fibers.

High-resolution XPS spectra of Fe 2p (Fig. 7a and b) for $CuFe_2O_4$ show distinct peaks at 710.9 eV and 724.4 eV, corresponding to Fe $2p_{3/2}$ and Fe $2p_{1/2}$,[38] respectively. These are deconvoluted into Fe^{2+} and Fe^{3+} oxidation states, indicating the mixed-valence nature of Fe ions. The Cu 2p spectrum shows peaks at 932.5 eV and 952.3 eV, attributed to Cu^{+} and Cu^{2+} states,[39] further confirming the coexistence of both oxidation states in $CuFe_2O_4$. For $NiFe_2O_4$ (Fig. 7c and d), the Fe 2p spectrum exhibits similar multiple splitting as $CuFe_2O_4$, while the Ni 2p spectrum reveals peaks at 855.5 eV (Ni $2p_{3/2}$) and 873.0 eV (Ni $2p_{1/2}$), which are characteristic of Ni^{2+} and Ni^{3+} species.[40] In generally, Ni^{2+} is often the predominant species in $NiFe_2O_4$, with Ni^{3+} often present as minor traces. For Ni^{3+} species can arise from surface oxidation, non-stoichiometry associated with cation vacancies, and redox interactions between Ni and Fe during synthesis.[41]

The C 1s spectrum of MBF-Cu and MBF-Ni (Fig. 8a and 9a) exhibits a dominant peak at 284.8 eV, corresponding to sp^2-hybridized C=C or C–C bonds. A minor peak observed at 282.1 eV is attributed to metal-carbon (M-C) interactions, and peak observed at 286.2 eV is assigned to C–O bonds, indicating the presence of hydroxyl or ether functional groups on the surface.[42] The O 1s spectra (Fig. 8b and 9b) show peak at 528.3 eV is associated O_2^{2-}, which contains Si–O–Si bonds, peak at 530.2 eV corresponds to lattice oxygen bonded to metal atoms (M–O), confirming the formation of metal oxide phases. A peak at 532.4 eV is assigned to surface hydroxyl groups (O–H).[43] For N 1s spectra (Fig. 8c and 9c), show contributions from metal–nitrogen (M–N) bonds at 397.3 eV, C=N–C bonds at 398.9 eV, and pyrrolic nitrogen at 400.2 eV, which contributes to surface activity and functional group interactions.[44] The high-resolution Fe 2p and Cu 2p spectra in MBF-Cu (Fig. 8d and e), as well as Fe 2p and Ni 2p in MBF-Ni (Fig. 9d and e), demonstrate similar mixed-valence

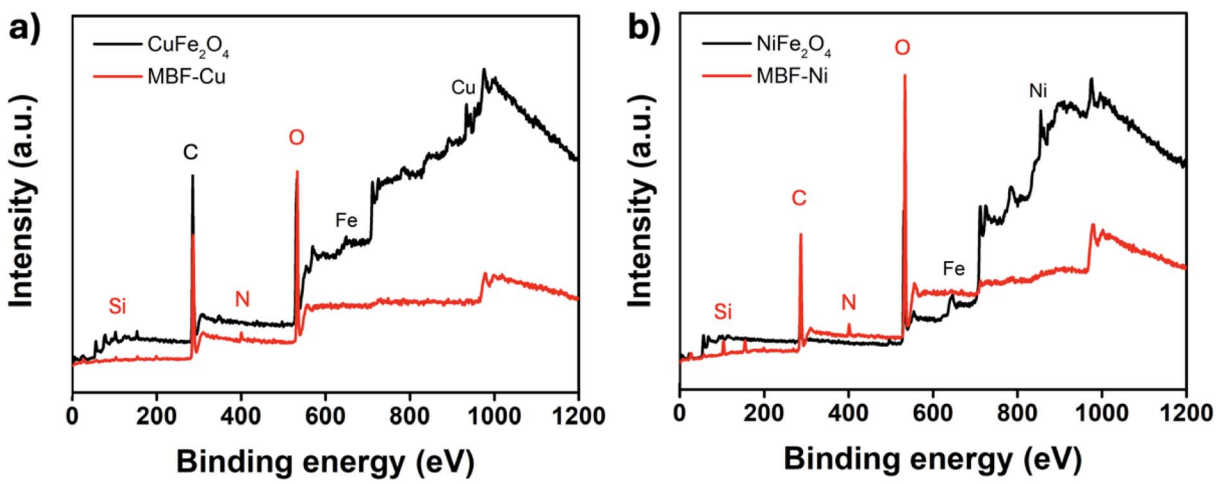

Fig. 6 XPS survey of (a) $CuFe_2O_4$ and MBF-Cu, (b) $NiFe_2O_4$ and MBF-Ni.

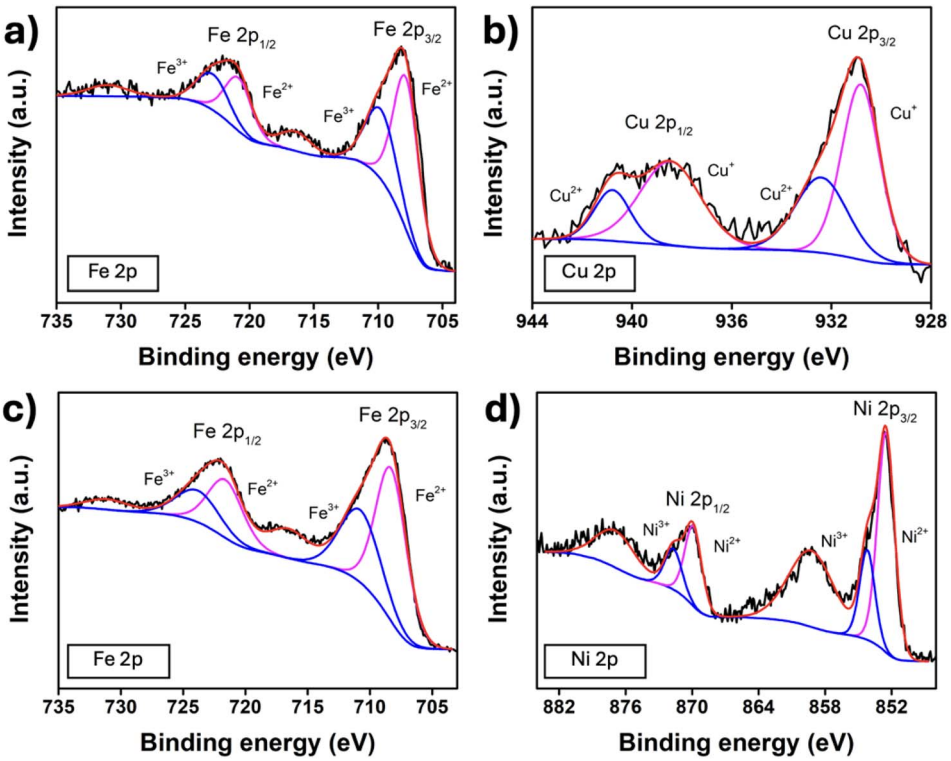

Fig. 7 High-resolution XPS analyses of MBF-Cu (a) Fe 2p, (b) Cu 2p, and MBF-Ni (c) Fe 2p, (d) Ni2p.

characteristics as their bulk metal ferrite counterparts.[38–40] The coexistence of multiple oxidation states in the transition metals is crucial for catalytic and redox applications.[45] The Si 2p peaks (Fig. 8f and 9f) show contributions from Si–OH at 100.0 eV, Si–O–Si at 100.8 eV, and Si^{3+} at 102.0 eV, indicating the incorporation of silica onto the MBF surface.[46,47]

3.6 Magnetic properties

In the Fig. 10a, calcined $CuFe_2O_4$ demonstrates a saturation magnetization at 64.24 emu g^{-1}. After coating with SiO_2 on $CuFe_2O_4$, the magnetization drops to 34.28 emu g^{-1}, exhibiting the same effects of isolation and dilution.[48] Addition of PEI again helps to slightly restore the magnetic performance 248.30

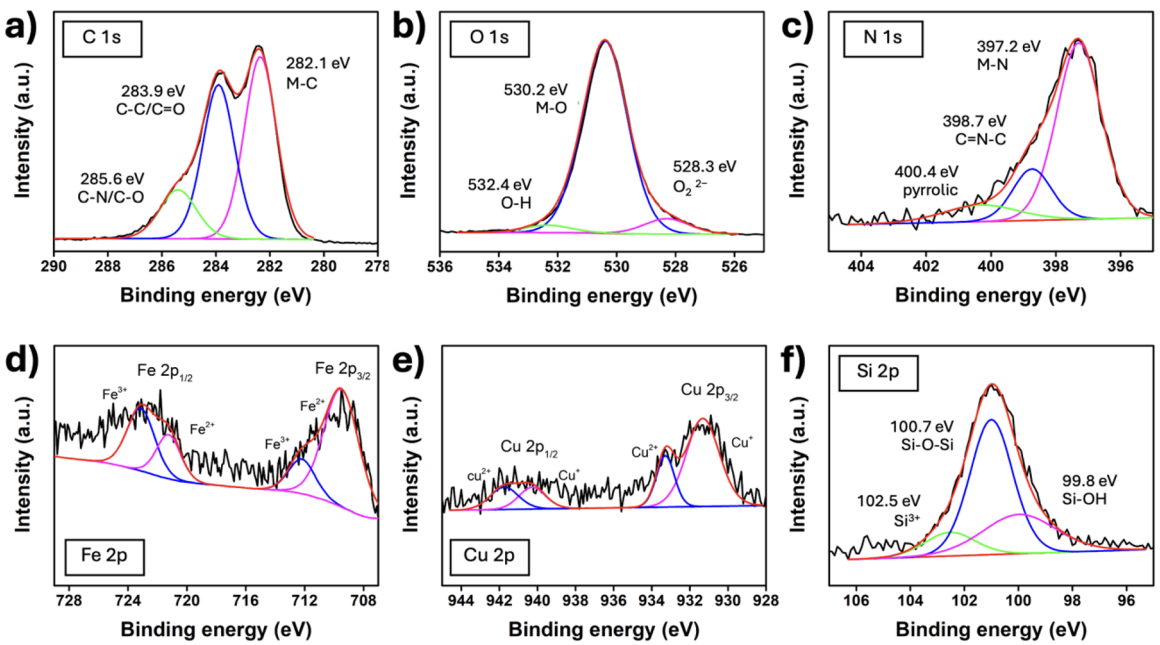

Fig. 8 High-resolution XPS analyses of MBF-Cu (a) C 1s, (b) O 1s, (c) N 1s, (d) Fe 2p, (e) Cu 2p, and (f) Si 2p.

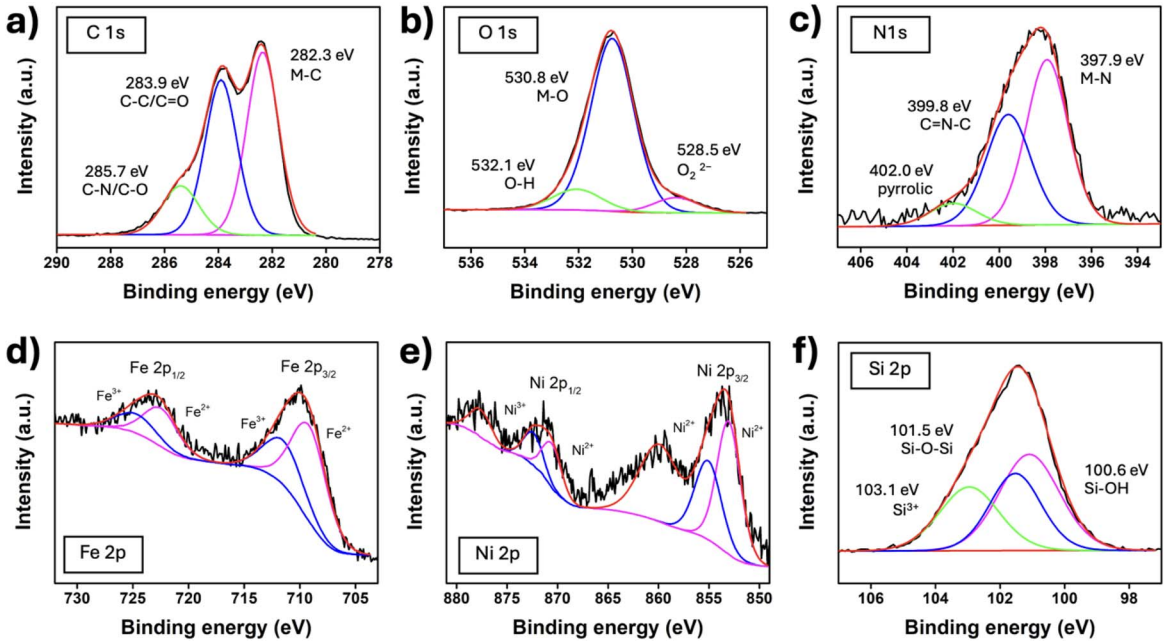

Fig. 9 High-resolution XPS analyses of MBF-Ni (a) C 1s, (b) O1s, (c) N 1s, (d) Fe 2p, (e) Ni 2p, and (f) Si 2p.

emu g^{-1}, supporting the role of PEI in enhancing particle dispersion. The MBF-Cu composite shows magnetic response 7.23 emu g^{-1}, indicating a dominant non-magnetic component. $NiFe_2O_4$ shows higher magnetic response at 106.89 emu g^{-1}, while $NiFe_2O_4$–SiO_2 and $NiFe_2O_4$–SiO_2-PEI show magnetic response 62.23 emu g^{-1} and 81.61 emu g^{-1}, respectively.

For the MBF-Ni, displays a reduced magnetization at 19.62 emu g^{-1} might of the composite nature of the material. All samples maintain adequate magnetic response for possible magnetic separation applications despite the decrease in saturation magnetization (M_s), which is essential for environmental or biological use.[49,50] The squareness ratio (SQ) was estimated in the following eqn (2),[51]

$$\text{Squareness ratio} = M_r/M_s \quad (2)$$

where M_r is remanent magnetization and M_s is saturation magnetization of samples. In this study, the SQ values remains near zero for all samples, confirming their soft magnetic nature, which is desirable for rapid magnetization and demagnetization cycles.[52] The magnetic measurements provide information about the magnetic parameters including, saturation magnetization (M_s), remanent magnetization (M_r), coercivity (H_c) and squareness ratio (SQ) which are shown in Table 2.

3.7 Chemical stability

Assessing the material's chemical stability in a range of chemical conditions is crucial for environmental remediation and catalytic applications.[53] Following exposure, the sample was collected, dried, and then analyzed using XRD analysis. The diffraction pattern (Fig. 11) was entirely unchanged, suggesting that neither

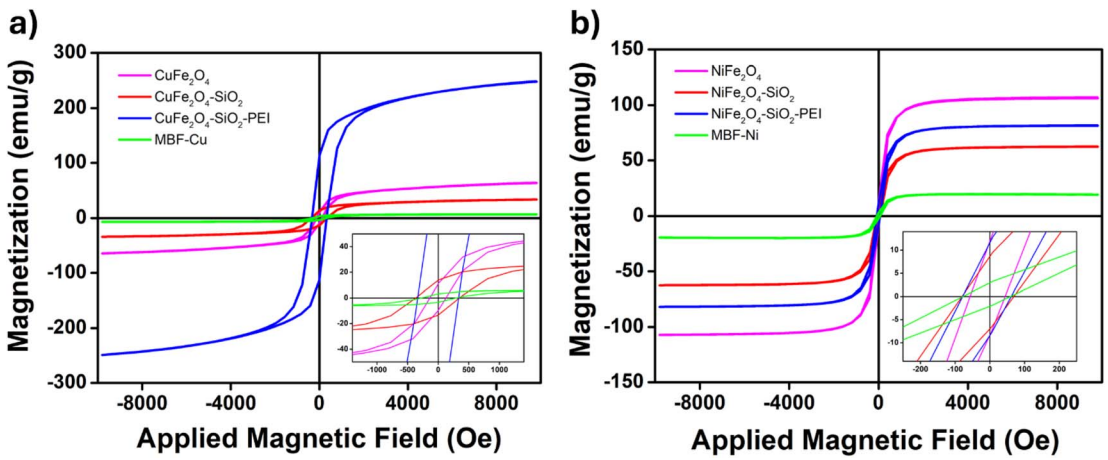

Fig. 10 VSM result of (a) $CuFe_2O_4$, $CuFe_2O_4$–SiO_2, $CuFe_2O_4$–SiO_2-PEI and MBF-Cu, (b) $NiFe_2O_4$, $NiFe_2O_4$–SiO_2, $NiFe_2O_4$–SiO_2-PEI and MBF-Ni.

Table 2 Magnetic properties of ferrite nanoparticles and modified bamboo fibers (MBF)

Sample	M_s	M_r	H_c	SQ
$CuFe_2O_4$	64.24	11.20	125.76	0.17
$CuFe_2O_4$–SiO_2	34.28	13.61	346.14	0.40
$CuFe_2O_4$–SiO_2-PEI	248.30	111.38	333.25	0.45
MBF-Cu	7.23	3.22	293.26	0.45
$NiFe_2O_4$	106.89	11.68	44.16	0.11
$NiFe_2O_4$–SiO_2	62.23	8.60	68.90	0.14
$NiFe_2O_4$–SiO_2-PEI	81.61	11.56	61.21	0.14
MBF-Ni	19.62	2.94	59.23	0.15

the composite structure nor the ferrite framework's crystalline topology were impacted.[54] This confirms that the material possesses excellent chemical resistance and structural stability, which is crucial for long-term use in diverse chemical environments. However, MBF-Cu and MBF-Ni immersed in hydrochloric acid showed a narrower and higher peak at 22.1° 2θ than the peak of other solvents. It was due to Cl^- ions penetrate the cellulose fibers and hydrolyze the amorphous region of samples.[55] From the above results, it was revealed that MBF-Ni has better chemical stability than MBF-Cu, which show the major peak of ferrite nanoparticles totally and clearly. Therefore, MBF-Ni was chosen for use as a filter in dyes filtration in the application part.

3.8 Selectivity of filters for dyes removal

The comparison of ABF and MBF-Ni filters for dye filtration was conducted to evaluate and compare their adsorption efficiency, filtration performance, and overall effectiveness in removing dye contaminants from aqueous solutions. From result in Fig. 12a–c show MBF-Ni (blue curve) demonstrated the best removal of CR, followed by MB and MO dye, respectively, while ABF (red curve) shown the maximum efficiency against only MB dye.

3.9 Effect of solution volume and concentration of CR for filtration efficiency and adsorption cycle

In Fig. 13a, the result shown that the absorbance spectra of CR solutions after filtered decreased when quantity of MBF-Ni in the column height increased. Higher loadings of MBF-Ni in column may enhanced the contact surface area and facilitating stronger interactions with the dye molecules. However, using too much filter cartridge may affect to flow of dyes solution. Therefore, the column fixed height 4 cm (0.15 g) of MBF-Ni filter was determined to be the optimal height for CR filtration. The bar graph in Fig. 13b illustrates the effect of CR concentration and CR solution volume on MBF-Ni filter. For adsorption test of the MBF-Ni filter were conducted using 10 and 20 mg L^{-1} CR dye, according to earlier reports, wastewater from industrial sources usually contains dye concentrations in the range of 10–200 mg L^{-1}.[56] From result, the MBF-Ni filter makes high filtration efficiency at concentrations 10 and 20 mg L^{-1}, the absorbance are very low might because of most of the dye molecules were effectively removed from the solution. However, when the concentration increases to 50 and 100 mg L^{-1}, the absorbance was increase, it suggesting that more dye remains in the filtrate and thus less was removed. When a high concentration of dye is filtered through a large column, the adsorption of the filter reaches saturation, allowing the unabsorbed dye molecules to pass through column, which make filtered solution still contains a large amount of dye.[57] Additionally, the experiment was

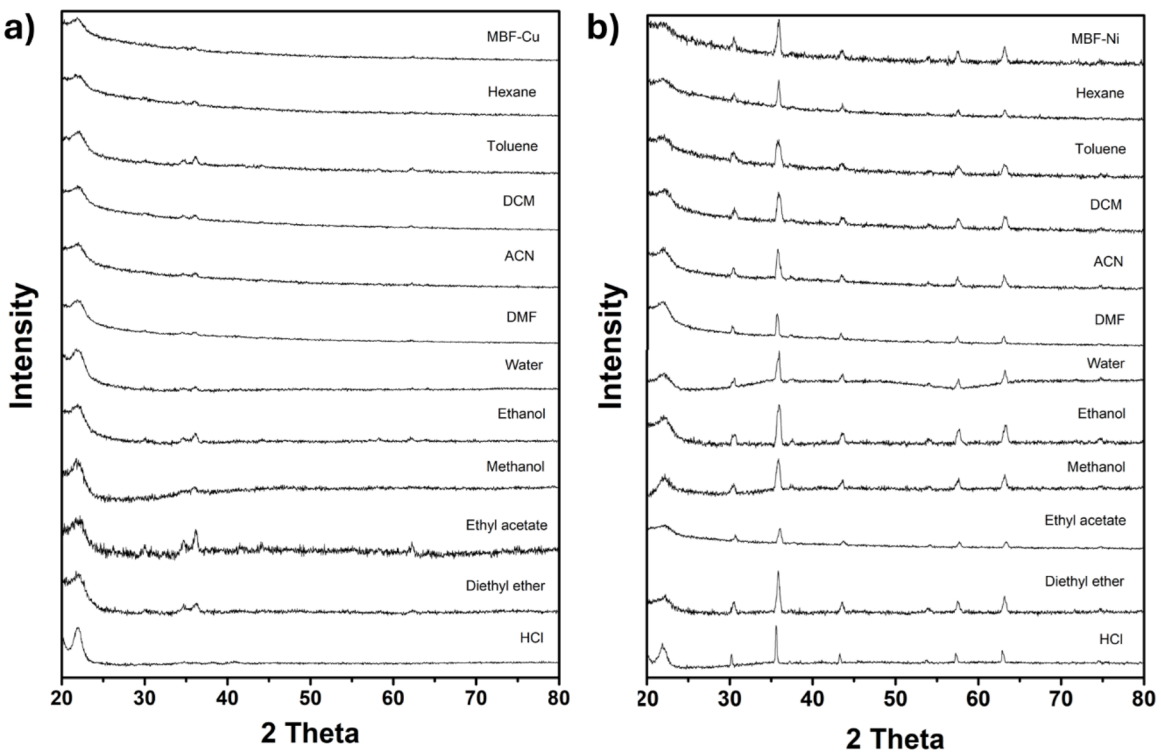

Fig. 11 XRD spectra of (a) MBF-Cu and (b) MBF-Ni after treated using various solvents.

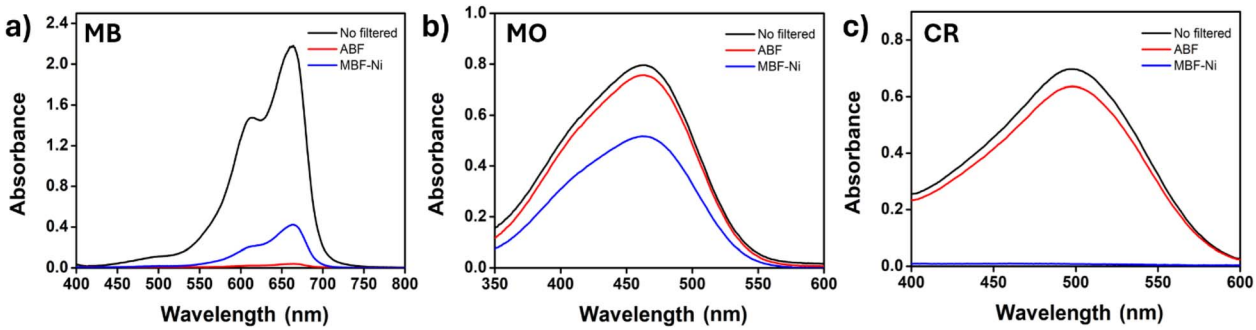

Fig. 12 UV-vis spectra of (a) Methylene Blue (MB), (b) Methyl Orange (MO), and (c) Congo Red (CR) solutions after filtered by ABF and MBF-Ni column.

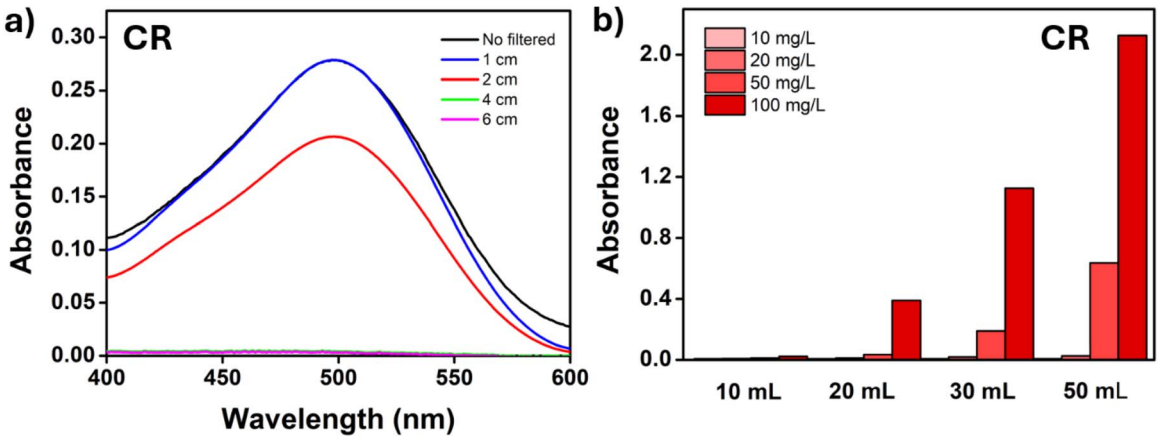

Fig. 13 (a) UV-vis spectra of Congo Red (CR) solutions after filtered through 1, 2, 4 and 6 cm height of MBF-Ni filter, (b) effect of volume and concentration on the absorbance of CR after filtered by MBF-Ni.

further conducted by filtering the dye with concentration of 10 mg L^{-1} using the dye volume of more than 100 mL, it was found that the MBF-Ni filter still has good filtration efficiency. The dye solution after filtering is clear and colorless. It was discovered that the maximum solution removal was reached before reaching removal efficiency of roughly 50–60%, as indicated in Table 3.

3.10 Removal efficiency and adsorption capacity of MBF-Ni filter

The removal efficiency (%) and adsorption capacity of MBF-Ni were calculated based on the initial and final concentrations of CR before and after filtration. As shown in Table 4, the removal efficiency (%) represents the percentage of dye removed from the solution and was calculated using the eqn (3),[58]

$$\text{Removal efficiency (\%)} = ((C_0 - C_f)/C_0) \times 100 \quad (3)$$

where C_0 is initial concentration, C_f is final concentration of CR (mg L^{-1}), respectively.

The adsorbed mass (mg) was determined by multiplying this concentration difference by the solution volume, was determined using the eqn (4),

$$\text{Adsorbed mass (mg)} = (C_0 - C_f) \times V \quad (4)$$

where C_0 is initial concentration, C_f is final concentration of CR (mg L^{-1}), and V is the volume of the dye solution (L), respectively.

The adsorption capacity, which indicates the amount of dye adsorbed per unit mass of adsorbent, was determined using the eqn (5),

$$\text{Adsorption capacity (mg g}^{-1}) = ((C_0 - C_f)/m) \times V \quad (5)$$

Table 3 Adsorption cycle, absorbance, and removal efficiency of MBF-Ni filter

Concentration of CR	Adsorption cycle (20 mL per cycle)	Absorbance (a.u.)	Removal efficiency (%)
10 mg L^{-1}	1	0.000	92.71
	2	0.000	92.43
	5	0.005	91.58
	10	0.027	88.37
	20	0.084	76.27
	25	0.139	60.73
20 mg L^{-1}	1	0.000	90.71
	2	0.000	90.56
	5	0.015	85.84
	10	0.093	83.65
	20	0.157	77.47
	25	0.324	53.51

Table 4 Removal efficiency, adsorbed mass and adsorption capacity of MBF-Ni filter (1 cycle)

Concentration of CR	Removal efficiency (%)	Adsorbed mass (mg)	Adsorption capacity (mg g^{-1})
10 mg L^{-1}	91.03	0.211	1.41
20 mg L^{-1}	90.90	0.383	2.56
50 mg L^{-1}	49.20	0.482	3.21
100 mg L^{-1}	39.65	0.796	5.32

where m is the adsorbent mass (g).

The MB-Ni filter developed in this study exhibited a high Congo Red removal efficiency of 90.90%, outperforming several recently reported (Table 5). These results, combined with the use of sustainable bamboo fibers and the amine-rich PEI coating, position MBF-Ni as an efficient, eco-friendly, and easily recoverable candidate for anionic dye remediation.[60–64]

3.11 Regeneration of ABF and MBF-Ni filter

The regenerated efficiency of ABF and MBF-Ni filters was evaluated by reusing the materials after chemical regeneration. Specifically, ABF was regenerated by soaking in 0.1 M HCl solution, while MBF-Ni was regenerated using 0.1 M NaCl solution. After regeneration, the filters were subsequently reused for the removal of methylene blue (MB) and Congo red (CR), respectively. The adsorption performance was tested at two different initial dye concentrations, 10 mg L^{-1} and 20 mg L^{-1}, to assess the effectiveness of the regeneration process under varying loading conditions.

As shown in Fig. 14, both MB and CR exhibited relatively low absorbance values across all tested solution volumes after filtration, indicating that a significant portion of the dyes had been effectively removed by the regenerated filters. Although a slight increasing trend in absorbance was observed with increasing volume. This may be attributed to the gradual saturation of active adsorption sites or limited mass transfer efficiency at higher solution volumes.

3.12 Adsorption kinetics

The adsorption kinetics were evaluated using pseudo-first-order and pseudo-second-order. Kinetic parameters (in Table 6) was performed using pseudo-first-order and the pseudo second-order kinetic models, following eqn (6) and (7),[63] respectively

$$\ln(q_e - q_t) = \ln q_e - k_1 t \quad (6)$$

Table 5 Comparison related to magnetic and adsorption parameters of CR on MBF-Ni with previous study

Adsorbent	Modified with	M_s (emu g^{-1})	Concentration (mg L^{-1})	Adsorption capacity (mg g^{-1})	% Removal	Ref.
$NiFe_2O_4$	—	—	20	—	85	M. B. Taj *et al.*, 2021 (ref. 59)
Porous fly ash	$NiFe_2O_4$	—	20	23.32	80–85	S. K. Sonar *et al.*, 2024 (ref. 60)
Cotton	$NiFe_2O_4$	45.57	—	89.45	78.70	C. Kong *et al.*, 2016 (ref. 61)
Exfoliated graphite	$NiFe_2O_4$	—	20	89.58	88.56	L. V. Tan *et al.*, 2020 (ref. 62)
Bamboo fibers	$NiFe_2O_4$–SiO_2-PEI	19.62	20	2.56	90.90	This study

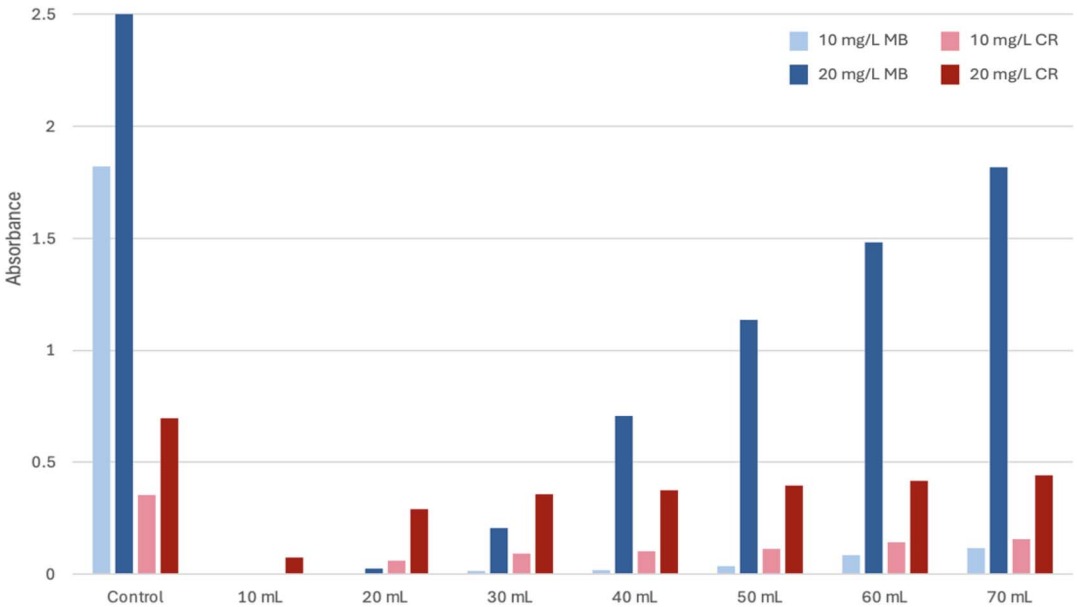

Fig. 14 The absorbance values of dye solutions after filtration through regenerated filters: methylene blue (MB) after filtration through the ABF filter (light blue and dark blue bar graphs), and Congo red (CR) after filtration through the MBF-Ni filter (pink and red bar graphs).

Table 6 Pseudo-first-order and pseudo-second-order kinetic model parameters for the adsorption of MB on ABF and CR on MBF-Ni

		Sample	
Model	Parameter	ABF	MBF-Ni
Pseudo-first-order	$q_{e(cal)}$ (mg g^{-1})	2.13	2.43
	k_1 (min^{-1})	0.0271	0.0381
	R^2	0.3539	0.8653
Pseudo-second-order	$q_{e(cal)}$ (mg g^{-1})	1.18	5.83
	k_2 (g mg^{-1} min^{-1})	0.0320	0.0297
	R^2	0.4602	0.9660

$$t/q_t = (1/k_2 q_e^2) + (t/q_e) \quad (7)$$

where q_e and q_t (mg g^{-1}) is adsorption capacity at equilibrium and in time (min), respectively. k_1 (min^{-1}) and k_2 (g mg^{-1} min^{-1}) is adsorption rate constants of the pseudo-first-order and the pseudo second-order kinetic models, respectively.

Fig. 15a show relatively poor linearity for both MBF-Ni and ABF, suggesting that the pseudo-first-order model does not adequately describe the adsorption process. In contrast, the plots of $1/q_t$ against time (Fig. 15b) exhibit much better linear fitting particularly for MBF-Ni, it indicating that the adsorption follows pseudo-second-order kinetics. This result implies that electron transfer between adsorbent and adsorbate or *vice versa* is the rate-limiting step, where adsorption depends on active sites and charge interactions.[64]

The isotherm models were performed using Langmuir and Freundlich model, following eqn (8) and (9), respectively

$$q_e = q_m(k_L C_e/(1 + k_L C_e)) \quad (8)$$

$$q_e = k_F C_e^{1/n} \quad (9)$$

where q_e (mg g^{-1}) is adsorption capacity at equilibrium. C_e (mg L^{-1}) is the equilibrium CR concentration. k_L (L mg^{-1}) and k_F (mg g^{-1}) (L mg^{-1})$^{1/n}$ is the Langmuir constant and the Freundlich constant, respectively. n is the relative distribution of energy and the heterogeneity of the adsorbate sites.

Both ABF and MBF-composite possess the Langmuir isotherm models. Fig. 15c and d showed fitting of C_e/q_e *versus* C_e

Table 7 Isotherm parameters of the adsorption of MB on ABF and CR on MBF-Ni

		Sample	
Model	Parameter	ABF	MBF-Ni
Langmuir	k_L (L mg^{-1})	−0.151	−0.298
	q_m (mg g^{-1})	1.18	5.83
	R^2	0.9919	0.8338
Freundlich	k_f (mg$^{1-(1/n)}$ L$^{1/n}$ g^{-1})	~0	~0
	$q_{e(cal)}$ (mg g^{-1})	—	—
	n	0.0044	0.112
	R^2	0.4173	0.2135

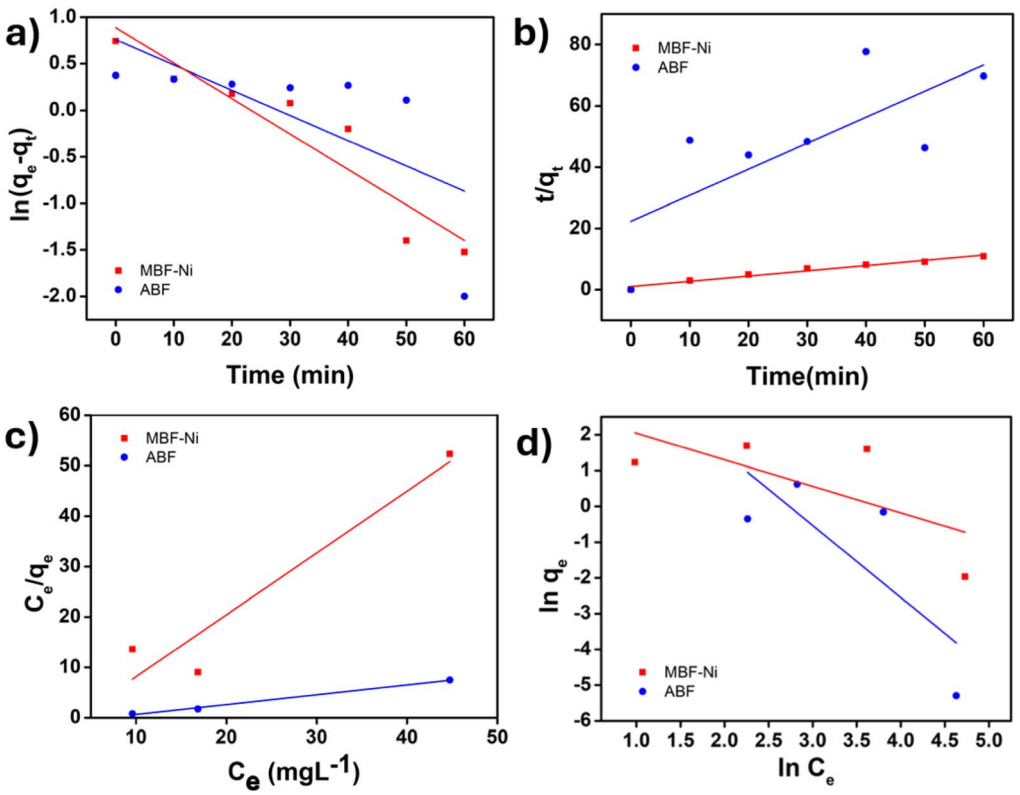

Fig. 15 Adsorption kinetics model (a) pseudo-first-order, (b) pseudo-second-order, and adsorption isotherm (c) Langmuir and (d) Freundlich for adsorption CR on the MBF-Ni and MB on the ABF filter.

Table 8 Comparison related to adsorption kinetic parameters of CR on MBF-Ni with previous study

Adsorbent	q_e (mg g^{-1})	k_2 (g mg^{-1} min^{-1})	%Removal	Ref.
$FANiFe_{50}$	23.33	0.0010	80–85	S. K. Sonar *et al.*, 2024 (ref. 60)
NFO500	45.97	0.0225	78.70	C. Kong *et al.*, 2016 (ref. 61)
$Co_{0.5}Mn_{0.5}Fe_2O_4$	20.0952	0.0372	93.85	Zhang *et al.*, 2024 (ref. 66)
MBF-Ni	5.83	0.0297	90.90	This study

and ln q_e *versus* ln C_e, respectively, Based on the R^2 value, this result indicates that the adsorption system follows Langmuir monolayer adsorption[65,66] between adsorbent and CR under the studied conditions. As shown in Table 7, maximum adsorption capacity (q_m) of ABF and MBF-composite are occurred at 1.18 and 5.83 (mg g^{-1}), respectively. Although MBF-Ni shows a lower q_e relative to pure nanostructured adsorbents, its superior %R value and eco-friendly composition offer a strategic advantage for industrial applications necessitating rapid contaminant removal when compare with previous study as show in Table 8.

Overall, the results suggest that the prepared adsorbents are not effective for Congo Red removal under the current experimental conditions. Future studies should focus on optimizing key parameters such as solution pH, adsorbent dosage, and surface functionalization to enhance the availability of active sites and improve electrostatic attraction between adsorbent and dye molecules.

3.13 Adsorption mechanisms analysis

To elucidate the adsorption performance and underlying mechanisms, the interactions between the MBF-Ni or ABF filters and the dye molecules were systematically investigated. For MBF-Ni filter, the presence of SiO_2 and PEI introduces a high density of amine functional groups, including NH_2 and protonated NH_3^+ groups, which significantly enhance the positive surface charge of the MBF-Ni filter, particularly under neutral to acidic conditions. In Fig. 16, interactions between MBF-Ni and CR is principally driven by electrostatic interactions between the negatively charged sulfonate groups of CR and the positively charged NH_2 and NH_3^+ groups loaded on the SiO_2 surface.[67] For ABF filter, the surface of alkali-treated bamboo fiber developed O^- and COO^- groups,[68] which resulted in a pronounced negative charge, resulting in a strong electrostatic interaction to the MB. Meanwhile, the repulsion force between the negative surface and the anionic dyes like MO and CR results in very low adsorption of both dyes caused by electrostatic interaction.[69] This adsorption process is identified as chemisorption, which is consistent with the TGA analysis (in Section 3.2) showing an endothermic behaviour. This suggests the formation of strong chemical interactions between the adsorbate and active sites on MBF-Ni. Furthermore, these findings are in good agreement with the pseudo-second-order kinetic model, which assumes that the adsorption rate is controlled by chemisorption between adsorbent and dyes molecules.[70] As a result, dye molecules are immobilized on the adsorbent surface and removed from the solution phase. Furthermore, in systems incorporating magnetic ferrite components, the separation process can be greatly simplified. The regeneration of ABF (using HCl) and MBF-Ni (using NaOH) effectively restored the adsorption performance of the filters. This is attributed to the desorption of dye molecules from the

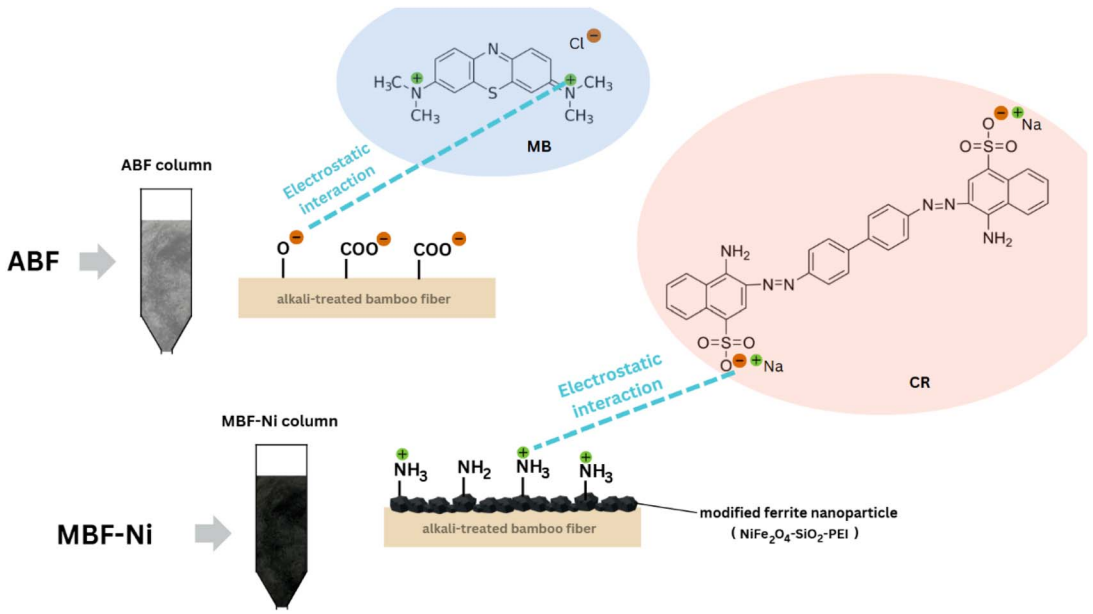

Fig. 16 Interactions between MBF-Ni and Congo Red (CR), and ABF and Methylene Blue (MB).

active sites through protonation (HCl) and ion-exchange effects (NaCl), which weaken the electrostatic interactions between the adsorbent and adsorbate.[71] Overall, these findings demonstrate that ABF and MBF-Ni filters possess good regeneration ability and can be reused multiple times without significant loss of adsorption efficiency.

4 Conclusion

$CuFe_2O_4$ and $NiFe_2O_4$ nanoparticles were successfully incorporated on bamboo fibers in this study, then followed coating by silica and surface modification with polyethyleneimine (PEI) to produce magnetic bamboo fiber composite (MBF). The MBF-Cu and MBF-Ni show surface functionality, thermal stability, and soft magnetic qualities which appropriate for use in environmental cleanup and magnetic separation applications. The excellent chemical stability of the MBF-Ni composites ensures their structural integrity and reusability under harsh chemical environments, which is critical for filter applications in dyes treatment systems. We use MBF-Ni as a filter of column for dyes filtration. The results indicate that MBF-Ni filter was crucial to maximize removal of Congo Red (CR) while compare with Methylene Blue (MB) and Methyl Orange (MO). MBF-Ni filter suitable for filtered large molecule dyes, which can support the filtration of dyes concentration 10–20 mg L^{-1}. The removal efficiency of CR had occurred with 90.90% and adsorption capacity (filtered method) was presented with 2.56 (mg g^{-1}). In addition, MBF-Ni have possessed pseudo-second-order kinetic model and Langmuir behavior with maximum adsorption capacity (q_m) at 5.83 (mg g^{-1}). Overall, MBF-Ni might be effective in removing CR dyes wastewater from factories with great remove efficiency, good flow and friendly for the environment, which might use for wide filtration applications in the future.

Author contributions

Writing – original draft, and investigation, R. K.; resources, C. S., K. C. C., and N. L.; writing – review and editing, supervision, and conceptualization, P. P.

Conflicts of interest

We wish to confirm that there are no known conflicts of interest associated with this publication.

Data availability

The datasets generated and analyzed during the current study are available from the corresponding author upon reasonable request.

Supplementary information (SI) is available. See DOI: https://doi.org/10.1039/d5ra10014c.

Acknowledgements

The authors would like to thank Center of Excellence for Innovation in Chemistry (PERCH-CIC), and the Department of Chemistry, Faculty of Science, Khon Kaen University for providing research facilities. This work has received funding support from the Fundamental Fund of Khon Kaen University from National Science, Research and Innovation Fund or NSRF, Thailand.

References

1 S. Yadav, K. S. Tiwari, C. Gupta, M. K. Tiwari, A. Khan and S. P. Sonkar, *Results Chem.*, 2023, **5**, 100733.
2 E. Ersöz and O. Altintas Yildirim, *J. Korean Ceram. Soc.*, 2022, **59**, 655–670.
3 J. Sachin, N. Singh, R. Singh, K. Shah and B. K. Pramanik, *Chemosphere*, 2023, **327**, 138497.
4 T. Islam, Md. R. Repon, T. Islam, Z. Sarwar and M. M. Rahman, *Environ. Sci. Pollut. Res.*, 2022, **30**, 9207–9242.
5 K. Ueda, J. Ohyama and A. Satsuma, *ACS Omega*, 2017, **2**, 3135–3143.
6 M. Lakshman, *J. Synth. Chem.*, 2022, **1**, 148–154.
7 H. Maati, O. Amadine, Y. Essamlali, S. Aboulhrouz, I. Jioui, K. Dânoun and M. Zahouily, *RSC Adv.*, 2023, **13**, 19617–19626.
8 N. Wang, H. Zhou, J. Ren, G. Gao, G. Zhao, Y. Yang, H. Wang and J. Wang, *Coatings*, 2023, **13**, 334.
9 M. Gharagozlou, M. Ghahari and M. Heydari, *Nanochem. Res.*, 2023, **8**, 1–22.
10 P. Yu, J. Xing, J. Tang, Z. Wang, C. Zhang, Q. Wang, X. Xiao and W. Huang, *J. Colloid Interface Sci.*, 2024, **661**, 164–174.
11 Y. K. Buchman, E. Lellouche, S. Zigdon, M. Bechor, S. Michaeli and J.-P. Lellouche, *Bioconjugate Chem.*, 2013, **24**, 2076–2087.
12 P. Yu, J. Xing, J. Tang, Z. Wang, C. Zhang, Q. Wang, X. Xiao and W. Huang, *J. Colloid Interface Sci.*, 2024, **661**, 164–174.
13 M. R. Esfahani, A. Taylor, N. Serwinowski, Z. J. Parkerson, M. P. Confer, I. Kammakakam, J. E. Bara, A. R. Esfahani, S. N. Mahmoodi, N. Koutahzadeh and M. Z. Hu, *ACS Sustainable Chem. Eng.*, 2020, **8**, 4225–4235.
14 S. Tang, L. Jiang, B. Ma, C. Tang, Y. Wen, N. Zhang, Y. Zhang and S. Su, *Cellulose*, 2020, **27**, 5089–5100.
15 L. S. Lobo and S. A. C. Carabineiro, *C*, 2020, **6**, 18.
16 Y. Miyah, A. Lahrichi, R. Kachkoul, G. El Mouhri, M. Idrissi, S. Iaich and F. Zerrouq, *Arab J. Basic Appl. Sci.*, 2020, **27**, 248–258.
17 S. Vermani, P. Kaur and V. Kaur, *J. Electron. Mater.*, 2024, **53**, 1796–1806.
18 H. Chen, Y. Yu, T. Zhong, Y. Wu, Y. Li, Z. Wu and B. Fei, *Cellulose*, 2017, **24**, 333–347.
19 O.-A. O. Abiodun, O. Oluwaseun, O. K. Oladayo, O. Abayomi, A. A. George, E. Opatola, R. F. Orah, E. J. Isukuru, I. C. Ede, O. T. Oluwayomi, J. A. Okolie and I. A. Omotayo, *Clean Technol.*, 2023, **5**, 934–960.
20 S. Anandan, T. Selvamani, G. G. Prasad, A. M. Asiri and J. J. Wu, *J. Magn. Magn. Mater.*, 2017, **432**, 437–443.
21 F. Salehzadeh, M. Esmkhani, M. Zallaghi, S. Javanshir and M. G. Dekamin, *Sci. Rep.*, 2023, **13**, 8675.
22 H. Wu, B. Liu, Y. Qi, X. Qiu, L. Chen and Y. Qin, *ACS Catal.*, 2024, **14**, 16127–16139.

23 H. Kavas, N. Kasapoğlu, A. Baykal and Y. Köseoğlu, *Chem. Pap.*, 2009, **63**, 450–455.
24 M. Khalaj, S.-M. Khatami, M. Kalhor, M. Zarandi, E. T. Anthony and A. Klein, *Molecules*, 2023, **29**, 125.
25 W. Li, F. Guo, Y. Zhao and Y. Liu, *Nanomaterials*, 2022, **12**, 4063.
26 M. J. Iqbal, N. Yaqub, B. Sepiol and B. Ismail, *Mater. Res. Bull.*, 2011, **46**, 1837–1842.
27 S. Morteza Mostashari and H. Fallah Moafi, *J. Ind. Text.*, 2007, **37**, 31–42.
28 O. H. Piñeres, E. C. Salcedo, A. P. Herrera, J. H. Sánchez and G. C. Quintana, *Cellulose*, 2020, **27**, 3903–3918.
29 B. J. Rani, B. Saravanakumar, G. Ravi, V. Ganesh, S. Ravichandran and R. Yuvakkumar, *J. Mater. Sci.: Mater. Electron.*, 2025, **36**, 1059.
30 P. Sivakumar, R. Ramesh, A. Ramanand, S. Ponnusamy and C. Muthamizhchelvan, *J. Alloys Compd.*, 2013, **563**, 6–11.
31 M. Choupani and A. Gholizadeh, *Prog. Phys. Appl. Mater.*, 2021, **1**, 19–24.
32 S. Nam, Y. Liu, Z. He, D. J. Hinchliffe and D. Fang, *Agric. Environ. Lett.*, 2024, **9**, e20138.
33 T. Dippong, E. A. Levei and O. Cadar, *Materials*, 2021, **14**, 1139.
34 S. Naghash-Hamed, N. Arsalani and S. B. Mousavi, *ChemistryOpen*, 2022, **11**, e202200156.
35 A. Bajorek, C. Berger, M. Dulski, M. Zubko, S. Lewińska, K. Prusik, A. Ślawska-Waniewska, F. Grasset and N. Randrianantoandro, *Metall. Mater. Trans. A*, 2022, **53**, 1208–1230.
36 D. N. Ghaffar, M. M. Arman, S. I. El-Dek and R. Ramadan, *Appl. Phys. A*, 2024, **130**, 254.
37 S. A. Al Kiey, R. Ramadan and M. M. El-Masry, *Appl. Phys. A*, 2022, **128**, 473.
38 A. Gaumet, F. Caddeo, D. Loche, A. Corrias, M. Casula, A. Falqui and A. Casu, *Nanomaterials*, 2021, **11**, 2680.
39 C. Liu, X.-D. Zhang, J.-M. Huang, M.-X. Guan, M. Xu and Z.-Y. Gu, *ACS Catal.*, 2022, **12**, 15230–15240.
40 C. Solís, S. Somacescu, E. Palafox, M. Balaguer and J. M. Serra, *J. Phys. Chem. C*, 2014, **118**, 24266–24273.
41 Z. Xie, C. Zhang, X. He, Y. Liang, D. Meng, J. Wang, P. Liang and Z. Zhang, *Front. Chem.*, 2019, **7**, 539.
42 Z. Song, X. Sun, Y. Li, W. Tang, G. Liu, J. Shui, X. Liu and R. Yu, *ACS Appl. Mater. Interfaces*, 2021, **13**, 5266–5274.
43 D. Zala, A. K. Mishra, I. Mukhopadhyay and A. Ray, *Nanotechnology*, 2024, **35**, 295701.
44 B. Ren, J. Miao, Y. Xu, Z. Zhai, X. Dong, S. Wang, L. Zhang and Z. Liu, *J. Cleaner Prod.*, 2019, **240**, 118143.
45 N. Wang, R.-X. Wang, Z.-J. Li, R. Liu, H. Gao, H.-Y. Chen, R. Li, Y.-Z. Long and H.-D. Zhang, *ACS Appl. Nano Mater.*, 2023, **6**, 15063–15072.
46 J. W. Ma, W. J. Lee, J. M. Bae, K. S. Jeong, S. H. Oh, J. H. Kim, S.-H. Kim, J.-H. Seo, J.-P. Ahn, H. Kim and M.-H. Cho, *Nano Lett.*, 2015, **15**, 7204–7210.
47 A. Lakhonchai, A. Chingsungnoen, P. Poolcharuansin, N. Chanlek, S. Tunmee and U. Rittihong, *Mater. Res. Express*, 2022, **9**, 055604.
48 O. Stefanescu, G. Vlase, M. Barbu, P. Barvinschi and M. Stefanescu, *J. Therm. Anal. Calorim.*, 2013, **113**, 1245–1253.
49 A. Toghan, M. Khairy, E. M. Kamar and M. A. Mousa, *J. Mater. Res. Technol.*, 2022, **19**, 3521–3535.
50 R. Sadeghi, A. Sharifi, M. Orlowska and I. Huynen, *Micromachines*, 2020, **11**, 809.
51 M. Thavarani, M. C. Robert, N. Pavithra, S. B. Prasath, Y. B. Kannan and A. A. Ahamed, *Appl. Phys. A*, 2022, **128**, 659.
52 D. J. Patil and S. N. Behera, *Environ. Monit. Assess.*, 2023, **195**, 591.
53 J. Yang, W. Han, B. Jiang, X. Wang, Y. Sun, W. Wang, R. Lou, H. Ci, H. Zhang and G. Lu, *ACS Sens.*, 2022, **7**, 995–1007.
54 C. Ding, H. Zhao, X. Zhu and X. Liu, *Nanomaterials*, 2022, **12**, 2021.
55 U. P. Agarwal, S. A. Ralph, C. Baez, R. S. Reiner and S. P. Verrill, *Cellulose*, 2017, **24**, 1971–1984.
56 E. Forgacs, T. Cserháti and G. Oros, *Environ. Int.*, 2004, **30**, 953–971.
57 T. M. Subrahmanya, J. Widakdo, S. Mani, H. F. M. Austria, W.-S. Hung, M. H K, J. K. Nagar, C.-C. Hu and J.-Y. Lai, *J. Cleaner Prod.*, 2022, **349**, 131425.
58 Z. Yuan, J. Wang, Y. Wang, Q. Liu, Y. Zhong, Y. Wang, L. Li, S. F. Lincoln and X. Guo, *RSC Adv.*, 2019, **9**, 21075–21085.
59 M. B. Taj, M. D. F. Alkahtani, A. Raheel, S. Shabbir, R. Fatima, S. Aroob, R. Yahya, W. Alelwani, N. Alahmadi, M. Abualnaja, S. Noor, R. H. Ahmad and H. Alshater, *Sci. Rep.*, 2021, **11**, 5439.
60 S. K. Sonar, P. S. Niphadkar, S. Mayadevi and P. N. Joshi, *Mater. Chem. Phys.*, 2014, **148**, 371–379.
61 C. Kong, J. Li, F. Liu, Y. Song and P. Song, *Desalin. Water Treat.*, 2016, **57**, 11337–11347.
62 L. V. Tan, N. T. H. Tham and P. V. Thinh, *IOP Conf. Ser.: Mater. Sci. Eng.*, 2020, **991**, 012086.
63 H. Firmino, E. Nascimento, K. Costa, L. Arzuza, R. Araujo, B. Sousa, G. Neves, M. Morales and R. Menezes, *Materials*, 2025, **18**, 754.
64 Y. Ho, *J. Hazard. Mater.*, 2006, **136**, 681–689.
65 K. Y. Foo and B. H. Hameed, *Chem. Eng. J.*, 2010, **156**, 2–10.
66 X. Zhang, Y. Xia and Z. Wang, *PLoS One*, 2024, **19**, e0307055.
67 L. Xiao, J. Liu, F. Zhang, F. Qin, Y. Wang, Z. Qin, Y. Yang, Z. Dai, J. Zheng and B. Tang, *Polymers*, 2025, **17**, 1741.
68 H. Chen, W. Zhang, X. Wang, H. Wang, Y. Wu, T. Zhong and B. Fei, *J. Wood Sci.*, 2018, **64**, 398–405.
69 D. Robati, B. Mirza, M. Rajabi, O. Moradi, I. Tyagi, S. Agarwal and V. K. Gupta, *Chem. Eng. J.*, 2016, **284**, 687–697.
70 A. K. Schütz, A. Soragni, S. Hornemann, A. Aguzzi, M. Ernst, A. Böckmann and B. H. Meier, *Angew. Chem., Int. Ed.*, 2011, **50**, 5956–5960.
71 I. Ramadhan, L. Kurniasari and I. Hartati, *J. Chem. Process Mater. Technol.*, 2025, **4**, 36–43.